Supplementary Information for

Forward genetic analysis using OCT screening identifies *Sfxn3* mutations leading to progressive outer retinal degeneration in mice

Bo Chen,[1*†] Bogale Aredo,[1*] Yi Ding,[1*‡] Xin Zhong,[1¥] Yuanfei Zhu,[1§] Cynthia X. Zhao,[1] Ashwani Kumar,[2] Chao Xing,[2,3,4] Laurent Gautron,[5] Stephen Lyon,[6] Jamie Russell,[6] Xiaohong Li,[6] Miao Tang,[6] Priscilla Anderton,[6] Sara Ludwig,[6] Eva Marie Y. Moresco,[6] Bruce Beutler[6¶] and Rafael L. Ufret-Vincenty[1¶]

Rafael L. Ufret-Vincenty
Email: Rafael.Ufret-Vincenty@UTSouthwestern.edu

Bruce Beutler
Email: Bruce.Beutler@UTSouthwestern.edu

This PDF file includes:

Supplementary text
SI References
Figures S1 to S12
Tables S1-S2

www.pnas.org/cgi/doi/10.1073/pnas.1921224117

Materials and Methods

Animals. Both male and female *Sod1*$^{-/-}$*Park7*$^{-/-}$*Prkn*$^{-/-}$ triple KO mice 12-15 mo of age were included in the experiments for the validation of our screening protocol. In the forward genetics mutagenesis protocol, the mutagenized G0 C57BL/6J males were bred with C57BL/6J females, and the resulting G1 males were crossed with C57BL/6J females to produce G2 mice. G2 females were backcrossed with their G1 sires to yield G3 mice, which were screened for phenotypes (S24). This protocol produces pedigrees carrying an average total of 59 non-synonymous coding/splicing mutations; note that X chromosome mutations are not screened because they are not propagated to the G3 generation using this breeding scheme. Wild-type (WT) animals were screened together with G3 mice (ranging from 4 to 10 mo of age) that were, with respect to each mutation site, homozygous mutant, heterozygous, or homozygous for the C57BL/6J reference allele. All mice were bred and kept in a barrier animal facility at UTSW. They had free access to food and water and were exposed to normal lighting conditions, with 12-h-on/12-h-off cycles. Anesthesia before procedures was achieved with a ketamine-xylazine cocktail (100mg/kg-5mg/kg). A mixture (1:1) of tropicamide 1% solution (Alcon Laboratories, Inc. Fort Worth, TX, USA) and phenylephrine hydrochloride 2.5% solution (Alcon, Inc. Lake Forest, IL, USA) was used for pupil dilation.

Whole-exome Sequencing and Determination of Candidate Genes. Computation of single locus linkage was performed for every mutation in each pedigree using recessive, semidominant (additive), and dominant models of transmission by the program Linkage Analyzer, an R-based program (https://mutagenetix.utsouthwestern.edu/linkage_analysis/linkage_analysis.cfm). For each mutation, the null hypothesis of independence from each measured phenotype was tested. The output of automated mapping was, for each pedigree, a Manhattan plot of the P value of genotype-phenotype association calculated using recessive, semidominant, and dominant models of transmission for every mutation in the pedigree, as well as a scatter plot depicting the phenotypic performance of mice homozygous for the reference allele (REF), heterozygous for the mutation (HET), and homozygous for the mutation (VAR) at every one of the mutation sites. Superpedigree linkage analysis (S24) was performed when multiple alleles of individual genes were encountered in screening. When this occurred, pedigrees containing mice with identical or nonidentical allelic mutations were combined and analyzed as a single larger pedigree. This increases the power to detect causal relationships between mutations and phenotypes. The OCT parameters were continuous variables and were analyzed using a linear regression model to

assess linkage to specific mutations. To predict the effect of the mutations, we used two programs: PolyPhen-2 (S25) and a splice site prediction program (S24).

Generation of *Sfxn3* null mice using CRISPR/Cas9 targeting. A genotype-phenotype association with recessive inheritance was considered validated if the CRISPR generated knockout allele phenocopied the original ENU-induced mutation. As described previously (S24): "Female C57BL/6J mice were superovulated by injecting them with 6.5 U of pregnant mare's serum gonadotropin (PMSG; Millipore, 367222) and then 6.5 U of human chorionic gonadotropin (hCG; Sigma-Aldrich, C1063) 48 h later. The superovulated females were subsequently mated with C57BL/6JJcl male mice (The Jackson Laboratory) overnight. The following day, fertilized eggs were collected from the oviducts of the female mice, and in vitro transcribed Cas9 mRNA (50 ng/μL) and sgRNA (20–50 ng/μL) [*Sfxn3* sgRNA, 50 ng/μl; 5'- TGCTGAGTCATACACGTATT -3')] were injected into the pronucleus or cytoplasm of the fertilized eggs." A total of 158 injected embryos were cultured in M16 medium (Sigma-Aldrich) at 37°C in 5% CO_2. To generate mutant mice, 113 two-cell stage embryos were transferred into the ampulla of the oviduct (10–20 embryos per oviduct) of pseudo-pregnant Hsd:ICR (CD-1) female mice (Harlan Laboratories). Fifteen pups were born, and 2 mosaic females were bred further to produce the two knockout lines containing the mutations shown in Supporting Fig. S3.

Electroretinogram (ERG). A scotopic Ganzfeld ERG system (Phoenix Research Labs, Pleasanton, CA, USA) was used following protocols outlined by the company as described before (S26): briefly, "mice were dark-adapted overnight for 16 hours. After anesthesia and pupil dilation, mice were placed on a platform covered by a homeothermic heating blanket to maintain body temperature, and preparations were made under a dim red light. GenTeal (Novartis, East Hanover, NJ, USA) liquid gel was applied to each eye after anesthesia to prevent corneal drying and to establish contact between the cornea and the electrode (gold-plate objective lens). The reference and the ground electrodes (platinum needles) were subcutaneously inserted on top of the head and into the tail, respectively. Scotopic Ganzfeld ERGs were obtained in response to low (0.1 log cd.s.m^{-2}) and high (3.1 log cd.s.m^{-2}) flash intensities (the inter-stimulus interval was 0.7 sec and 60 sec for low and high flash intensities, respectively; flash duration was 1 msec). For analysis, the amplitude of the a-wave was measured from baseline to the most negative trough, whereas that of the b-wave was measured from the trough of the a-wave to the most positive peak of the retinal response." Mice were used at 3m and 5m old (n=3-4 per age group).

Histology of Retinal Sections. After enucleation, the right eyes were immediately placed in 2-ml tubes with holes and frozen in liquid nitrogen-cooled isopentane for 2 minutes (S27). The tubes were then quickly transferred to liquid nitrogen. After all eyes were collected, the tubes were transferred to a pre-cooled solution of methanol/acetic acid (97:3; in a -80°C freezer) in 50-ml tubes for freeze substitution for at least 48 h. The eyes were gradually warmed up to room temperature (first at -20°C for 24 h, then at 4°C for 4 h, and finally moved to RT). The eyes were then transferred to 100% ethanol for paraffin embedding using routine methods.

Images of the H&E sections from *Sfxn3*$^{-/-}$ and *Sfxn3*$^{+/+}$ control mice were taken at 20x magnification on either side of the optic nerve head using a Leica DM2000 microscope (Leica Microsystems, Wetzlar, Germany). The H&E images were then opened in ImageJ and the ONL thickness was measured (S28) at 100µm intervals starting from the optic nerve head (ONH) and up to a distance of 1000 µm on each side. Separately, the number of nuclei in a layer was counted in the same fashion. Three measurements were averaged at each point for each parameter.

Preparation and staining of RPE and retinal flat mounts. After enucleation, eyes were fixed in 4% PFA and processed as described before (S29). For RPE flat mounts the tissue was stained with anti ZO-1 primary antibody followed by a secondary antibody attached to Alexa Fluor 488 and imaged using confocal microscopy as detailed before (S35). To prepare retinal whole mounts, after removing the anterior tissues (cornea, lens and iris), the retina was post-fixed in cold methanol (-20^{0}C) for 1 hr and incubated with isolectin B4 (IB4) overnight at 4^{0}C following a previously described protocol (S36). The retinal flat mounts were imaged using a Leica DMI300B microscope equipped with a Hamamatsu camera as described before (S27).

RNAscope in situ hybridization. After cardiac perfusion with 4% PFA, eyes from 4 m old mice were collected and post-fixed overnight at 4ºC and processed routinely for paraffin embedding. In situ hybridization (ISH) was performed on paraffin embedded retinal sections using the RNAscope technique. To detect *Sfxn3* RNA expression in C57BL/6J mouse retinas, an appropriate RNAscope probe (Mn-Sfxn3-O1) was designed with the assistance of Advanced Cell Diagnostics (Hayward, CA, USA); the sequence is proprietary information of ACD. The probe consists of 20 oligo pairs. Each oligo has two hybridizing regions of 18-25 bases. The negative control sections were treated in the same way but were incubated with a bacterial dihydrodipicolinate reductase mRNA (dapB) probe. Stained sections were imaged on a Leica DM2000 microscope (Leica Microsysstems, Wetzlar, Germany) using a Jenoptik Gryphax CCD camera and acquired with Progress software (V.1.1.8.159).

Electron Microscopy (EM). After routine processing of the left eyes for electron microscopy, 70-nm-thin sections were cut (UTSW Electron Microscopy Core). These sections were stained with 2% aqueous uranyl acetate and lead citrate and imaged with a JEOL 1200EX II transmission electron microscope (JEOL USA, Inc., Peabody, MA, USA). ImageJ software (http://imagej.nih.gov/ij/) was used by a masked investigator for analysis (S29). Three *Sfxn3*$^{-/-}$ (n = 23 EM fields) and four *Sfxn3*$^{+/+}$ eyes (n = 34 EM fields) were analyzed. These EM fields were obtained in a masked and standardized fashion (the whole sample was scanned, and three EM fields were skipped between each photographed EM field).

Processing of retinal samples into single-cell suspensions. Eyes were collected from 4 C57BL/6J mice (4 mo old) and the retinas were peeled off from the posterior eyecups. A 2 mm trephine was centered on the optic disc spot and used to carefully and reproducibly isolate the central retina, which was placed in a solution containing 20 units/ml of activated papain with 0.005% DNase. After incubation for 45 minutes in a 37ºC water bath with agitation, the mixture was triturated 10-20 times and centrifuged at 300 x g for 5 minutes at room temperature. In order to reduce dissociation-induced acute, endogenous transcriptional alterations (S30), we applied the general transcription inhibitor, actinomycin D (ActD), (Sigma-Aldrich, Cat# A1410) at three steps during the dissociation process: to the papain solution at 45 mM, to the papain inhibitor solution at 45 mM, and during trituration at 3 mM (S31). After centrifugation, the supernatant was discarded, and the cell pellet was immediately resuspended in diluted DNase/albumin-ovomucoid inhibitor solution. The cell suspension was centrifuged at 70 x g for 6 minutes at RT. After centrifugation, the supernatant was completely removed and the cell pellet was resuspended in 100 µL of a dead cell-removal microbead suspension (Miltenyi Biotec, Auburn, CA, USA, No.130-090-101), which was then passed through the corresponding MS column (Miltenyi Biotec, No. 130-042-201) while applying an OctoMACS Separator containing a permanent magnet (Miltenyi Biotec, No. 130-042-109). The company-recommended 1× Binding Buffer was used to elute the live cell fraction. Finally, the live cell suspension was centrifuged down at 70 x g for 6 minutes at RT and the final pellet was resuspended in DPBS containing 0.4% BSA. Cell viability was determined using a cellometer (Nexcelom Bioscience LLC, Lawrence, MA, USA).

Analyses of single cell transcriptomes. Cell Ranger 3.0.0 (10X Genomics) was used to process the raw sequencing data obtained from the 10X Genomics. BCL files were converted to FASTQ files and aligned to mouse (mm10) reference transcriptome. Transcript counts of each

cell were quantified using the unique molecular identifier (UMI) and valid cell barcode. The gene expression matrix from cell ranger was used as input to the Seurat R package (v3.0.0) for downstream analysis (S32). Cells with less than 200 genes per cell and high mitochondrial gene content were filtered out. The global-scaling normalization method “LogNormalize” was used for normalization. A subset of genes exhibiting high variation across the single cells was determined. The highly variable genes were calculated using the “FindVariableFeatures” module in Seurat. For the sample, a Shared Nearest Neighbor (SNN) Graph was constructed with the “FindNeighbors” module in Seurat by determining the k-nearest neighbors of each cell. The clusters were then identified by optimizing SNN modularity using the “FindClusters” module. This allowed for a sensitive detection of rare cell types. We obtained 23 clusters with a resolution of 0.5. Clusters were named on the basis of known gene markers specific to various cell types found in the retina (S33).

Differential expression analysis of each cluster was performed in Seurat. Violin plots were generated using ggplot2 (v 3.1.0) in R (v3.5.0). Gene set enrichment and pathway analysis were performed using an R package clusterProfiler (S34); https://bioconductor.org/packages/release/bioc/html/clusterProfiler.html) and Ingenuity Pathway Analysis software (IPA) (QIAGEN, Redwood City, www.qiagen.com/ingenuity and https://www.qiagenbioinformatics.com/products/ingenuity-pathway-analysis/).

Statistical Analysis. Statistical analysis was done using SigmaPlot 11.0 (Systat Software, Inc. San Jose, CA, USA) and the data are presented as the mean ± standard error of mean (SEM). When comparing two groups, a two-tailed Student's t-test or the Mann-Whitney U test was performed. A P value < 0.05 was considered to be statistically significant. For scRNA-seq, average expression and dispersion per gene is calculated in a Seurat model and features are divided into bins to get z-scores for dispersion per bin. Data was then scaled, and dimensional reduction was performed with principle component analysis. The differential expression testing was performed using Wilcoxon Rank Sum test in Seurat.

SI References

S1. M. N. Preising, B. Görg, C. Friedburg, N. Qvartskhava, B. S. Budde, M. Bonus, M. R. Toliat, C. Pfleger, J. Altmüller, D. Herebian, M. Beyer, H. J. Zöllner, H. J. Wittsack, J. Schaper, D. Klee, U. Zechner, P. Nürnberg, J. Schipper, A. Schnitzler, H. Gohlke, B. Lorenz, D. Häussinger,

H. J. Bolz, Biallelic mutation of human SLC6A6 encoding the taurine transporter TAUT is linked to early retinal degeneration. *FASEB J*. 33(10):11507-11527 (2019).

S2. B. Heller-Stilb, C. van Roeyen, K. Rascher, H. G. Hartwig, A. Huth, M. W. Seeliger, U. Warskulat, D. Häussinger, Disruption of the taurine transporter gene (taut) leads to retinal degeneration in mice. *FASEB J*. 16(2):231-233 (2002).

S3. L. Xiang, X. J. Chen, K. C. Wu, C. J. Zhang, G. H. Zhou, J. N. Lv, L. F. Sun, F. F. Cheng, X. B. Cai, Z. B. Jin, miR-183/96 plays a pivotal regulatory role in mouse photoreceptor maturation and maintenance. *Proc Natl Acad Sci U S A*. 114(24):6376-6381 (2017).

S4. C. H. Xia, E. Lu, H. Liu, X. Du, B. Beutler, X. Gong, The role of Vldlr in intraretinal angiogenesis in mice. *Invest Ophthalmol Vis Sci.* 52(9):6572-9 (2011).

S5. J. R. Heckenlively, N. L. Hawes, M. Friedlander, S. Nusinowitz, R. Hurd, M. Davisson, B. Chang, Mouse model of subretinal neovascularization with choroidal anastomosis. *Retina*. 23(4):518-522 (2003).

S6. Y. Chen, Y. Hu,G. Moiseyev, K. K. Zhou, D. Chen, J. X. Ma, Photoreceptor degeneration and retinal inflammation induced by very low-density lipoprotein receptor deficiency. *Microvasc Res*. 78(1):119-27 (2009)

S7. W. H. Lee, H. Higuchi, S. Ikeda, E. L. Macke, T. Takimoto, B. R. Pattnaik, C. Liu, L. F. Chu, S. M. Siepka, K. J. Krentz, C. D. Rubinstein, R. F. Kalejta, J. A. Thomson, R. F. Mullins, J. S. Takahashi, L. H. Pinto, A. Ikeda, Mouse Tmem135 mutation reveals a mechanism involving mitochondrial dynamics that leads to age-dependent retinal pathologies. *Elife*. 5 (2016). pii: e19264.

S8. S. J. Bowne, Q. Liu, L. S. Sullivan, J. Zhu, C. J. Spellicy, C. B. Rickman, E. A. Pierce, S. P. Daiger, Why do mutations in the ubiquitously expressed housekeeping gene IMPDH1 cause retina-specific photoreceptor degeneration? *Invest Ophthalmol Vis Sci*. 47(9):3754-65 (2006).

S9. J. Birtel, T. Eisenberger, M. Gliem, P. L. Müller, P. Herrmann, C. Betz, D. Zahnleiter, C. Neuhaus, S. Lenzner, F. G. Holz, E. Mangold, H. J. Bolz, P. Charbel Issa, Clinical and genetic

characteristics of 251 consecutive patients with macular and cone/cone-rod dystrophy. *Sci Rep*. 8(1):4824 (2018).

S10. R. Sanuki, S. Watanabe, Y. Sugita, S. Irie, T. Kozuka, M. Shimada, S. Ueno, J. Usukura, T. Furukawa, Protein-4.1G-Mediated Membrane Trafficking Is Essential for Correct Rod Synaptic Location in the Retina and for Normal Visual Function. *Cell Rep*. 10(5):796-808 (2015).

S11. C. L. Cheng, R. S. Molday, Interaction of 4.1G and cGMP-gated channels in rod photoreceptor outer segments. *J Cell Sci*. 15;126(Pt 24):5725-5734 (2013).

S12. K. Baba, I. Piano, P. Lyuboslavsky, M. A. Chrenek, J. T. Sellers, S. Zhang, C. Gargini, L. He, G. Tosini, P. M. Iuvone, Removal of clock gene Bmal1 from the retina affects retinal development and accelerates cone photoreceptor degeneration during aging. *Proc Natl Acad Sci U S A.* 115(51):13099-13104 (2018).

S13. O. B. Sawant, A. M. Horton, O. F. Zucaro, R. Chan, V. L. Bonilha, I. S. Samuels, S. Rao, The Circadian Clock Gene Bmal1 Controls Thyroid Hormone-Mediated Spectral Identity and Cone Photoreceptor Function. *Cell Rep*. 21(3):692-706 (2017).

S14. A. Bulloj, A. Maminishkis, M. Mizui, S. C. Finnemann, Semaphorin4D-PlexinB1 Signaling Attenuates Photoreceptor Outer Segment Phagocytosis by Reducing Rac1 Activity of RPE Cells. *Mol Neurobiol*. 55(5):4320-4332 (2018).

S15. J. Assawachananont, S. Y. Kim, K. D. Kaya, R. Fariss, J. E. Roger, A. Swaroop, Cone-rod homeobox CRX controls presynaptic active zone formation in photoreceptors of mammalian retina. *Hum Mol Genet*. 27(20):3555-3567 (2018).

S16. N. M. Tran, A. Zhang, X. Zhang, J. B. Huecker, A. K. Hennig, S. Chen, Mechanistically distinct mouse models for CRX-associated retinopathy. *PLoS Genet*. 10(2):e1004111 (2014). doi: 10.1371/journal.pgen.1004111.

S17. J. F. Griffith, M. J. DeBenedictis, E. I. Traboulsi, A novel dominant CRX mutation causes adult-onset macular dystrophy. *Ophthalmic Genet*. 39(1):120-124 (2018).

S18. K. A. Wycisk, C. Zeitz, S. Feil, M. Wittmer, U. Forster, J. Neidhardt, B. Wissinger, E. Zrenner, R. Wilke, S. Kohl, W. Berger, Mutation in the auxiliary calcium-channel subunit CACNA2D4 causes autosomal recessive cone dystrophy. *Am J Hum Genet*. 79(5):973-977 (2006).

S19. K. A. Wycisk, B. Budde, S. Feil, S. Skosyrski, F. Buzzi, J. Neidhardt, E. Glaus, P. Nürnberg, K. Ruether, W. Berger, Structural and functional abnormalities of retinal ribbon synapses due to Cacna2d4 mutation. *Invest Ophthalmol Vis Sci*. 47(8):3523-3530 (2006).

S20. V. Kerov, J. G. Laird, M. L. Joiner, S. Knecht, D. Soh, J. Hagen, S. H. Gardner, W. Gutierrez, T. Yoshimatsu, S. Bhattarai, T. Puthussery, N. O. Artemyev, A. V. Drack, R. O. Wong, S. A. Baker, A. Lee, α(2)δ-4 Is Required for the Molecular and Structural Organization of Rod and Cone Photoreceptor Synapses. *J Neurosci*. 38(27):6145-6160 (2018).

S21. B. S. Clark, S. Cui, J. B. Miesfeld, O. Klezovitch, V. Vasioukhin, B. A. Link, Loss of Llgl1 in retinal neuroepithelia reveals links between apical domain size, Notch activity and neurogenesis. *Development.* 139(9):1599-1610 (2012).

S22. S. Hüttl, S. Michalakis, M. Seeliger, D. G. Luo, N. Acar, H. Geiger, K. Hudl, R. Mader, S. Haverkamp, M. Moser, A. Pfeifer, A. Gerstner, K. W. Yau, M. Biel, Impaired channel targeting and retinal degeneration in mice lacking the cyclic nucleotide-gated channel subunit CNGB1. *J Neurosci*. 25(1):130-138 (2005).

S23. P. A. Winkler, K. J. Ekenstedt, L. M. Occelli, A. V. Frattaroli, J. T. Bartoe, P. J. Venta, S. M. Petersen-Jones, A large animal model for CNGB1 autosomal recessive retinitis pigmentosa. *PLoS One*. 8(8):e72229 (2013). doi: 10.1371/journal.pone.0072229.

S24. T. Wang, X. Zhan, C.-H. Bu, S. Lyon, D. Pratt, S. Hildebrand, J. H. Choi, Z. Zhang, M. Zeng, K.-w. Wang, E. Turer, Z. Chen, D. Zhang, T. Yue, Y. Wang, H. Shi, J. Wang, L. Sun, J. SoRelle, W. McAlpine, N. Hutchins, X. Zhan, M. Fina, R. Gobert, J. Quan, M. Kreutzer, S. Arnett, K. Hawkins, A. Leach, C. Tate, C. Daniel, C. Reyna, L. Prince, S. Davis, J. Purrington, R. Bearden, J. Weatherly, D. White, J. Russell, Q. Sun, M. Tang, X. Li, L. Scott, E. M. Y.

Moresco, G. M. McInerney, G. B. K. Hedestam, Y. Xie, B. Beutler, Real-time resolution of point mutations that cause phenovariance in mice. Proc Natl Acad Sci U S A. 112, E440-9 (2015).

S25. I. A. Adzhubei, S. Schmidt, L. Peshkin, V. E. Ramensky, A. Gerasimova, P. Bork, A. S. Kondrashov, S. R. Sunyaev, A method and server for predicting damaging missense mutations. *Nat Methods.* 7(4),248-249 (2010).

S26. B. Chen, B. Aredo, Y. Zhu, Y. Ding, C. Xin-Zhao, R. L. Ufret-Vincenty, A Mouse Model of Retinal Recovery From Photo-Oxidative/Photo-Inflammatory Injury: Nrf2, SOD1, DJ-1, and Parkin Are Not Essential to Recovery. *Invest Ophthalmol Vis Sci*. 60(4),1165-1174 (2019).

S27. B. Aredo, K. Zhang, X. Chen, C. X. Wang, T. Li, R. L. Ufret-Vincenty, Differences in the distribution, phenotype and gene expression of subretinal microglia/macrophages in C57BL/6N (Crb1 rd8/rd8) versus C57BL6/J (Crb1 wt/wt) mice. *J Neuroinflammation*. 15, 12:6 (2015).

S28. X. Zhong, B. Aredo, Y. Ding, K. Zhang, C. X. Zhao, R. L. Ufret-Vincenty, Fundus Camera-Delivered Light-Induced Retinal Degeneration in Mice With the RPE65 Leu450Met Variant is Associated With Oxidative Stress and Apoptosis. *Invest Ophthalmol Vis Sci.* 57(13), 5558-5567 (2016).

S29. B. Aredo, T. Li, X. Chen, K. Zhang, C. X. Wang, D. Gou, B. Zhao, Y. He, Ufret-Vincenty RL. A chimeric Cfh transgene leads to increased retinal oxidative stress, inflammation, and accumulation of activated subretinal microglia in mice. *Invest Ophthalmol Vis Sci.* 56, 3427-3440 (2015).

S30. S. C. van den Brink, F. Sage, Á. Vértesy, B. Spanjaard, J. Peterson-Maduro, C. S. Baron, C. Robin, A. van Oudenaarden, Single-cell sequencing reveals dissociation-induced gene expression in tissue subpopulations. *Nat Methods*. 14(10), 935-936 (2017).

S31. Y. E. Wu, L. Pan, Y. Zuo, X. Li, W. Hong, Detecting Activated Cell Populations Using Single-Cell RNA-Seq. *Neuron.* 96(2), 313-329.e6 (2017).

S32. T. Stuart, A. Butler, P. Hoffman, C. Hafemeister, E. Papalexi, W.M. Mauck III, Y. Hao, M. Stoeckius, P. Smibert, R. Satija, Comprehensive Integration of Single-Cell Data. *Cell*, 177 (2019), 10.1016/j.cell.2019.05.031.

S33. E. M. Macosko, A. Basu, R. Satija, J. Nemesh, K. Shekhar, M. Goldman, I. Tirosh, A. R. Bialas, N. Kamitaki, E. M. Martersteck, J. J. Trombetta, D. A. Weitz, J. R. Sanes, A. K. Shalek, A. Regev, S. A. McCarroll, Highly Parallel Genome-wide Expression Profiling of Individual Cells Using Nanoliter Droplets. *Cell*. 161(5), 1202-1214 (2015).

S34. G. Yu, L. G. Wang, Y. Han, Q. Y. He, clusterProfiler: an R package for comparing biological themes among gene clusters*. OMICS.* 16(5), 284-287 (2012).

S35. Y. Ding, B. Aredo, X. Zhong, C. X. Zhao, R. L. Ufret-Vincenty, Increased susceptibility to fundus camera-delivered light-induced retinal degeneration in mice deficient in oxidative stress response proteins. *Exp Eye Res*. 159, 58-68 (2017).

S36. S. Tual-Chalot, K. R. Allinson, M. Fruttiger, H. M. Arthur, Whole mount immunofluorescent staining of the neonatal mouse retina to investigate angiogenesis in vivo. *J Vis Exp*. (77):e50546 (2013). doi: 10.3791/50546.

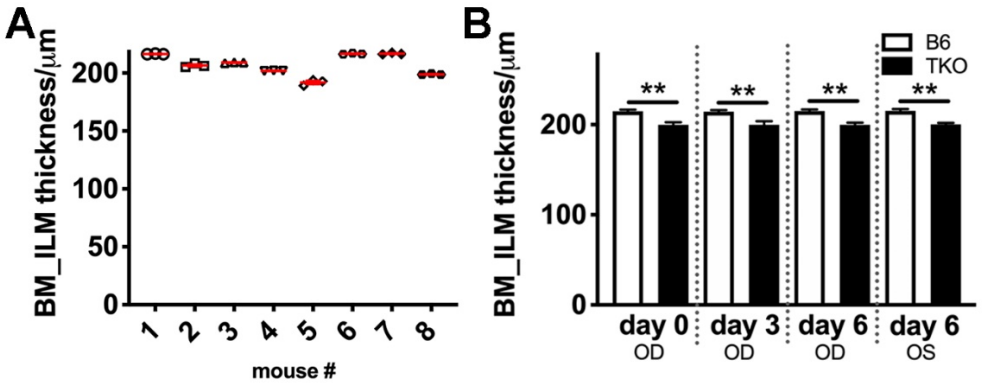

Fig. S1. Consistency and reproducibility of screening tools used in forward genetics study. We first tested the usefulness of our OCT measurements (A, B) in distinguishing mice with retinal anomalies. The images were obtained and analyzed by investigators masked to the genotype of the mice. (A) The high reproducibility of our assays is demonstrated when comparing total retinal thickness measurements. Four B6 controls and 4 TKO mice (deficient in SOD1, DJ-1 and Parkin) numbered randomly (masked) 1-8 on the x-axis were imaged on three different days (d0, d3, and d6). Three data points are shown for each mouse. The average CV was 0.42%. (B) At the end of the experiment the data were unmasked and organized by genotype. Measurements of retinal thickness (BM to ILM) on OCT images from TKO (n=4) and B6 control (n=4) mice taken at d0, d3, and d6 show consistency between days, and between eyes for both genotypes. OD, right eye; OS, left eye. Error bars represent the standard error of the mean for experimental groups. **p< 0.01, Student's t test.

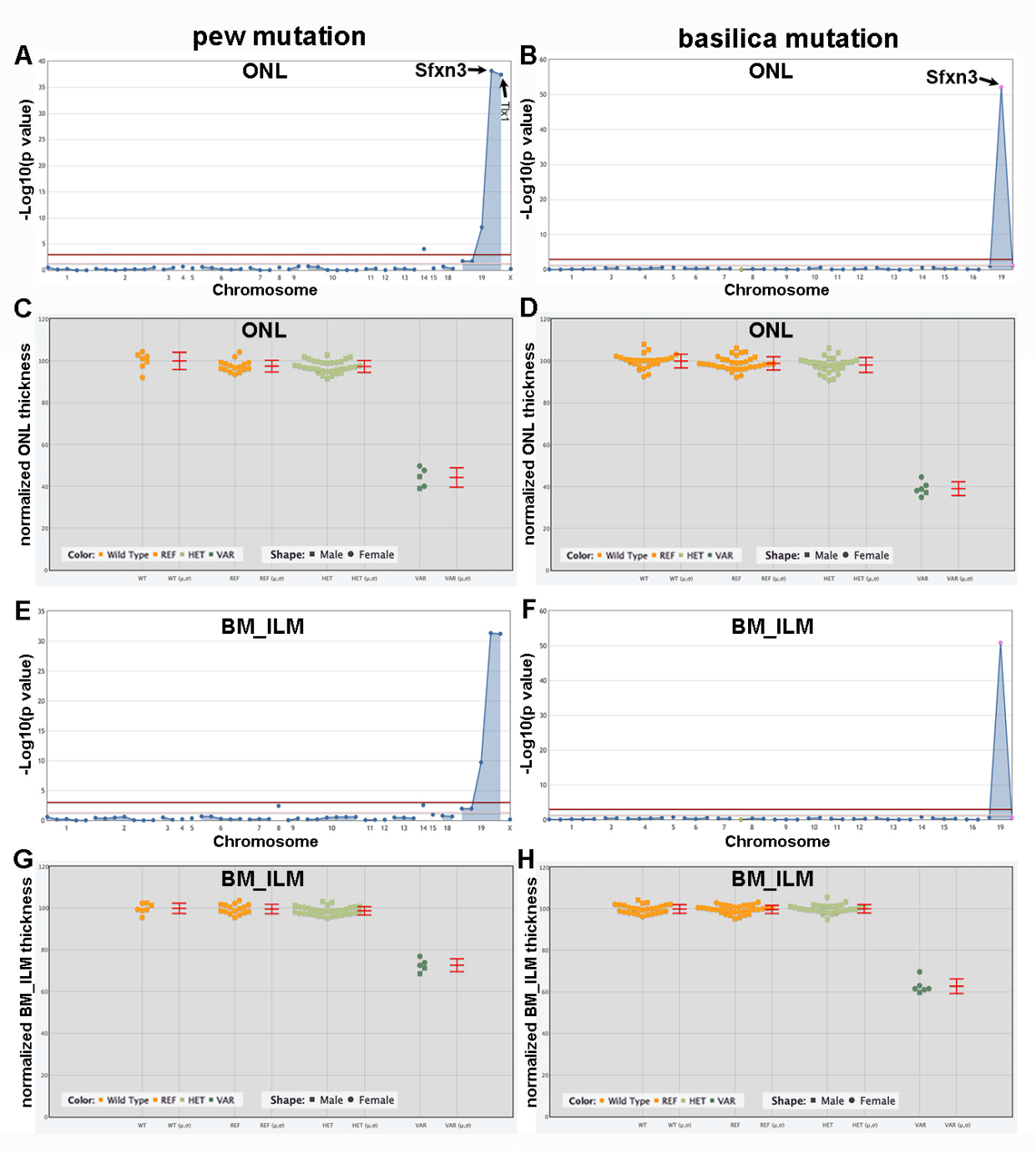

Fig. S2. Manhattan plots showing P values calculated using a recessive transmission model are shown for two *Sfxn3* mutations we named *pew* (A, E) and *basilica* (B, F). The -log10 P values (y axis) are plotted vs. the chromosomal positions of the mutations (x axis) identified in the G1 founders of each pedigree. The horizontal red line represents a threshold of P = 0.05 with Bonferroni correction. Quantitative phenolypic data (continuous variable data) from OCT measurements of ONL (A and B) and total retina (BM_ILM; E and F) were used for linkage analysis and show highly significant associations between the two *Sfxn3* mutations and these OCT parameters. The pedigree where the *pew* mutation was identified (left side panels) contained another mutation in linkage disequilibrium with *Sfxn3* (*Tlx1*). However, in the second pedigree (right side panels), the only mutation with a significant association with the OCT parameters was

the *basilica Sfxn3* mutation. Phenotwic data for ONL (C, D) and BM_ILM (G, H) is shown plotted vs. genotype at the *Sfxn3* mutation site for both *pew* (C, G) and *basilica* (D, H). Each data point represents one mouse. Mean (μ) and SD (σ) are indicated. Abbreviations; ONL - outer nuclear layer thickness. BM_ILM - Bruch's membrane to internal limiting membrane thickness.

A Sfxn3-1i mutation

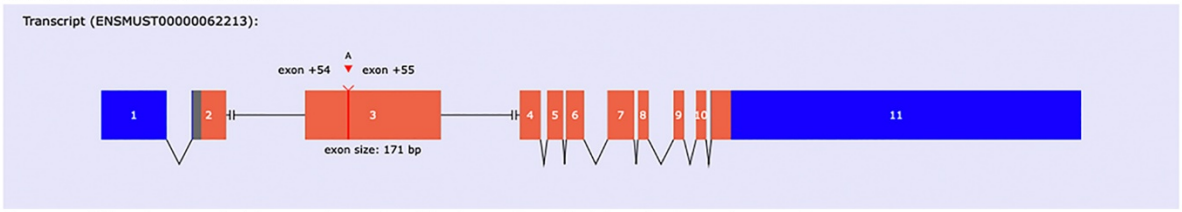

- the resulting transcript has a 1 nucleotide insertion that leads to a stop codon
- this predicts a protein product that is truncated at amino acid 71 (the normal protein is 321 amino acids long)

B Sfxn3-4d mutation

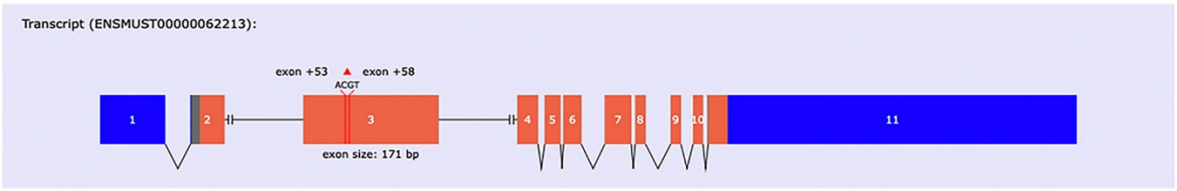

- the resulting transcript has a 4 nucleotide deletion
- this predicts a frame-shifted protein product beginning after amino acid 71 and terminating after the addition of 15 aberrant amino acids. The normal protein is 321 amino acids in length.

C Native Sfxn3:

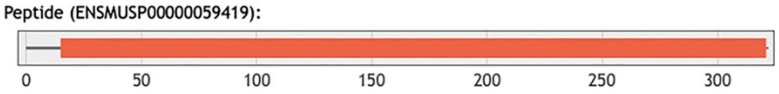

Figure S3. Mutations in the two CRISPR mouse lines compared to native Sfxn3.

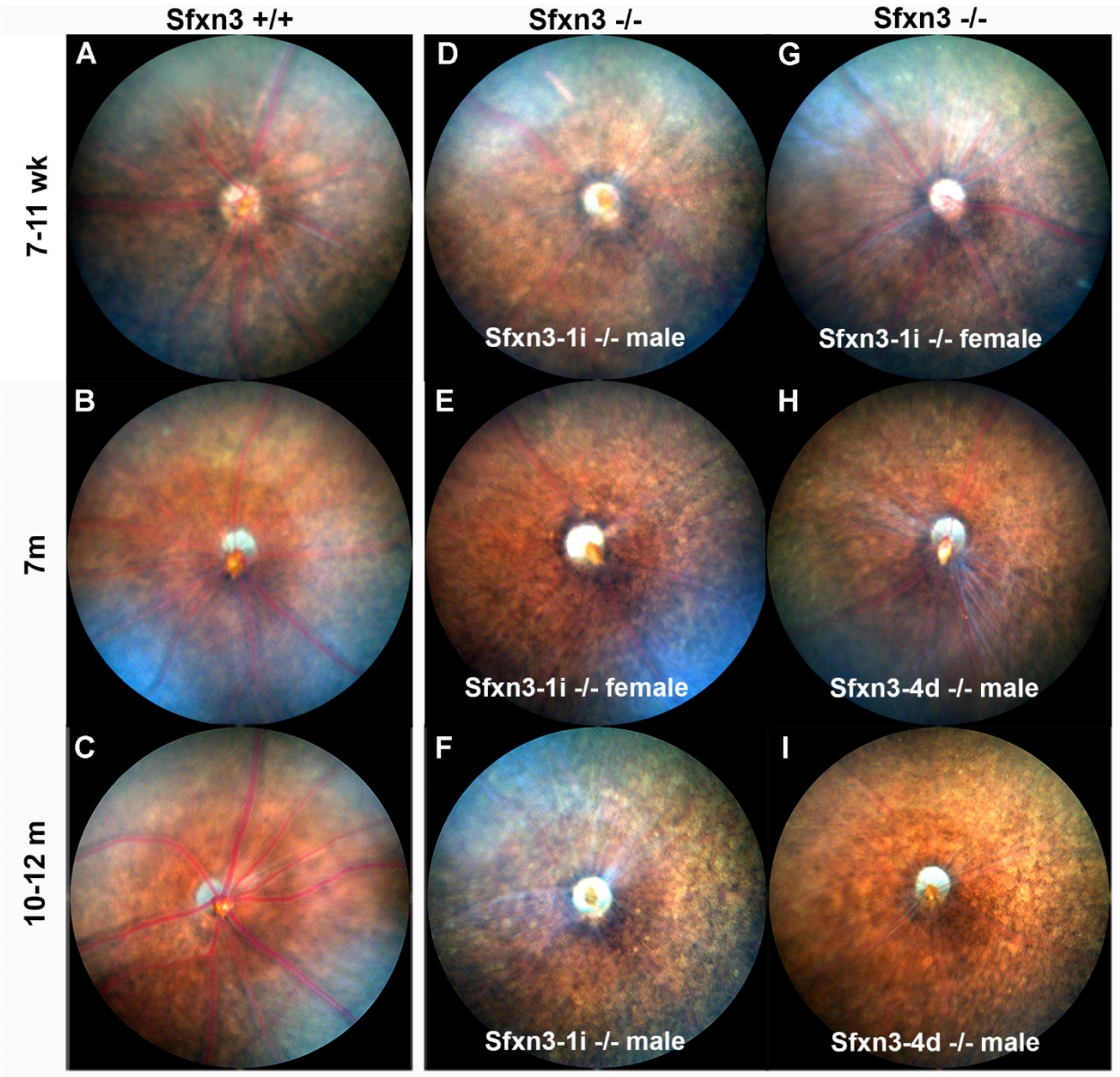

Fig. S4 Fundus images of CRISPR/Cas9-generated Sfxn3-/- mice show qualitatively abnormal vasculature and RPE mottling. Representative fundus photos of Sfxn3+/+ (A, B,C) and Sfxn3-/- (D-I) mice are depicted for three age groups (7-11 wks, 7 m and 10-12 m). Compared with Sfxn3+/+ controls, note the vascular attenuation in mice carrying two different mutations in Sfxn3: Sfxn3-1i -/- are homozygous for a 1bp insertion (D-G), while Sfxn3-4d-/- are homozygous for a 4 bp deletion (H,I). Compared to control mice, Sfxn3-/- mice also demonstrate RPE mottling that increases with age. We did not observe any effect of gender on the phenotype.

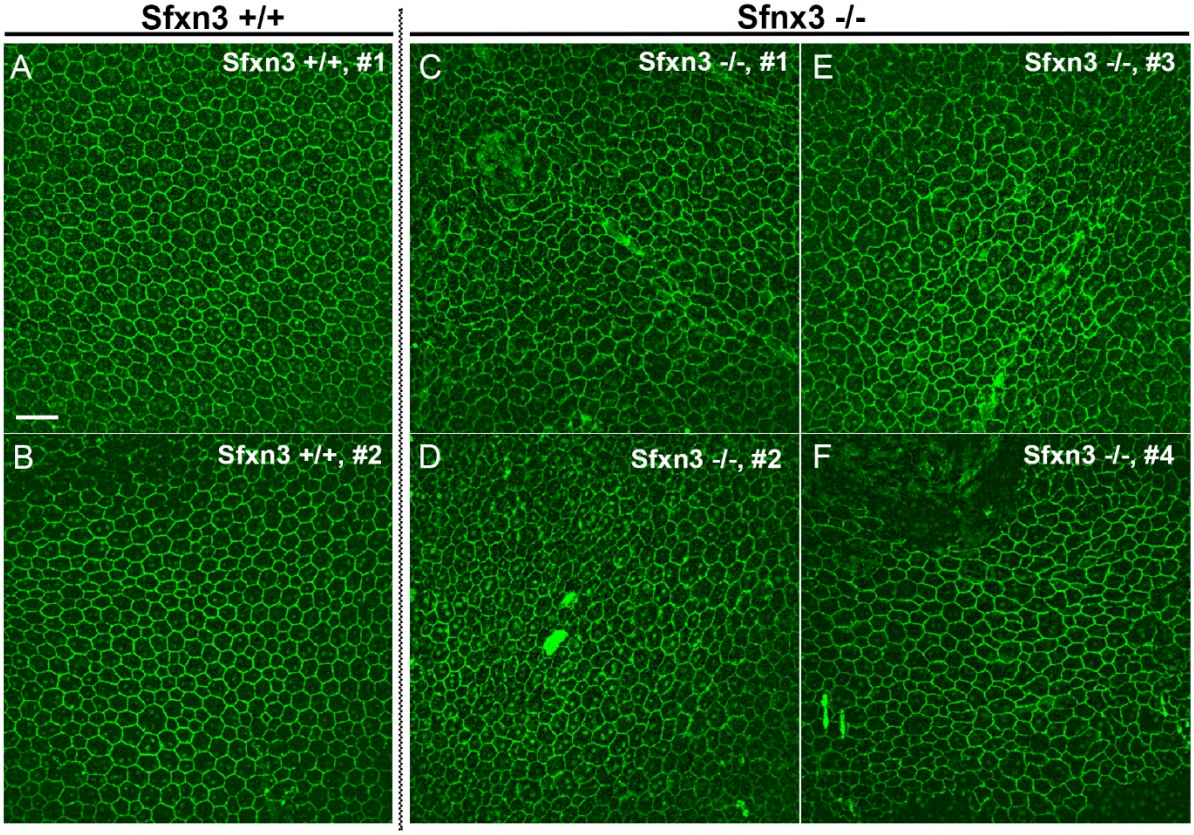

Fig. S5. ZO-1 staining of RPE flatmounts from two Sfxn3 +/+ (A, B) and four Sfxn3 -/- (C-F) mice. The mice were 10-12 months of age. The images were taken on a confocal microscope and were all obtained at a distance of 1 disc diameter from the disc. Note that while Sfxn3 +/+ RPE cells maintain a clear regular hexagonal shape, the RPE cells from Sfxn3-/- have a prominent disruption of this pattern (very irregular shapes), which is characteristic of sick/damaged RPE cells. Scale bar = 50 microns

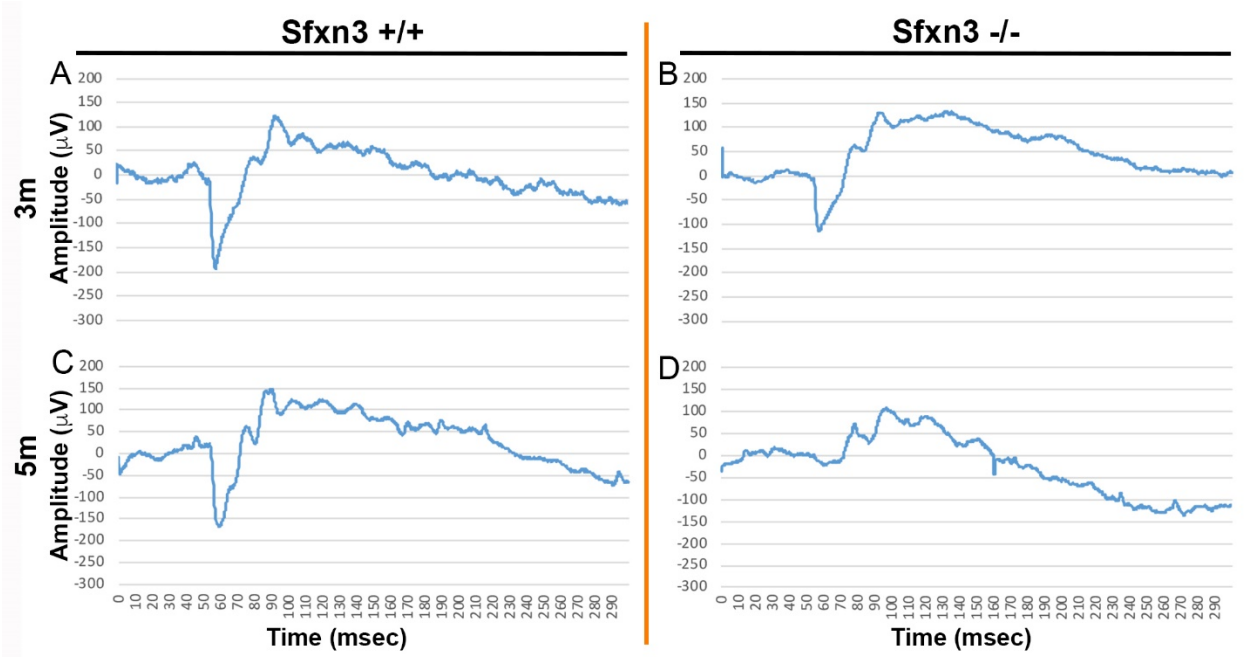

Fig. S6 Examples of scotopic electroretinograms (ERG; flash intensity = 3.1 log cd.s.m^{-2}) on Sfxn3 +/+ (A,B) and Sfxn3 -/- (C,D) mice at 3 months of age (A,C) and 5 months of age (B,D). A reduction in ERG amplitude is seen in Sfxn3 -/- by 3 m that becomes more striking by 5 months of age.

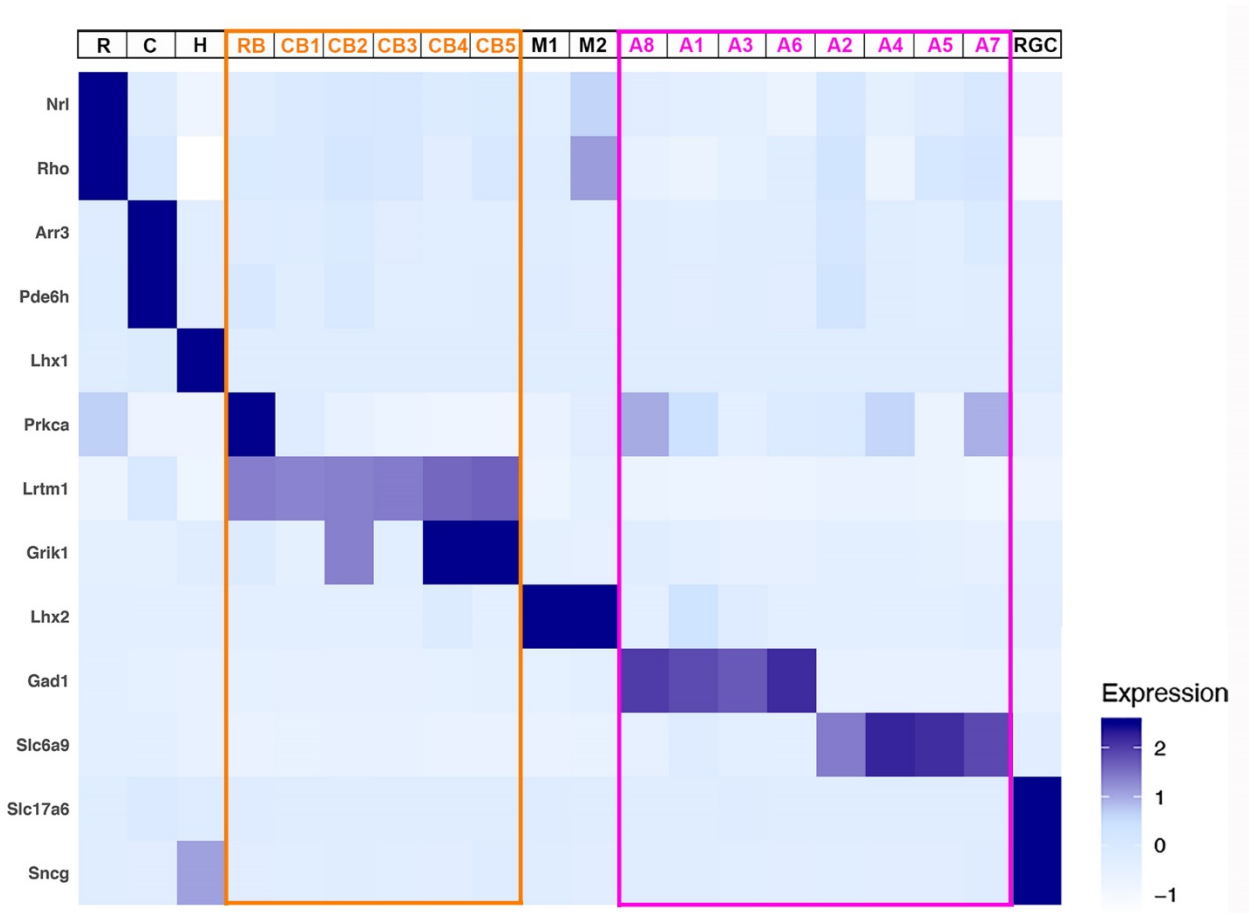

Fig. S7. Expression of published cell markers in our cell clusters. There is a very high correlation between published cell markers and the expected cell types in the clusters identified in our single cell RNA sequencing data. Markers are shown for rods (R: Nrl and Rho), cones (C: Arr3 and Pde6h), horizontal cells (H: Lhx1), rod bipolar cells (RB: Prkca and Lrtm1), cone bipolar cells (CB1-5: Lrtm1 for all bipolars and Grik1 for OFF cone bipolars), Muller cells (M1 and M2: Lhx2), amacrine cells (A1-8: Gad1 for GABAergic and Starburst amacrine cells, and Slc6a9 for Glycinergic amacrine cells), and retinal ganglion cells (RGC: Slc17a6 and Sncg). Clusters of bipolar cells (including rod bipolars) are included in the orange square, while clusters of amacrine cells are grouped in the pink square.

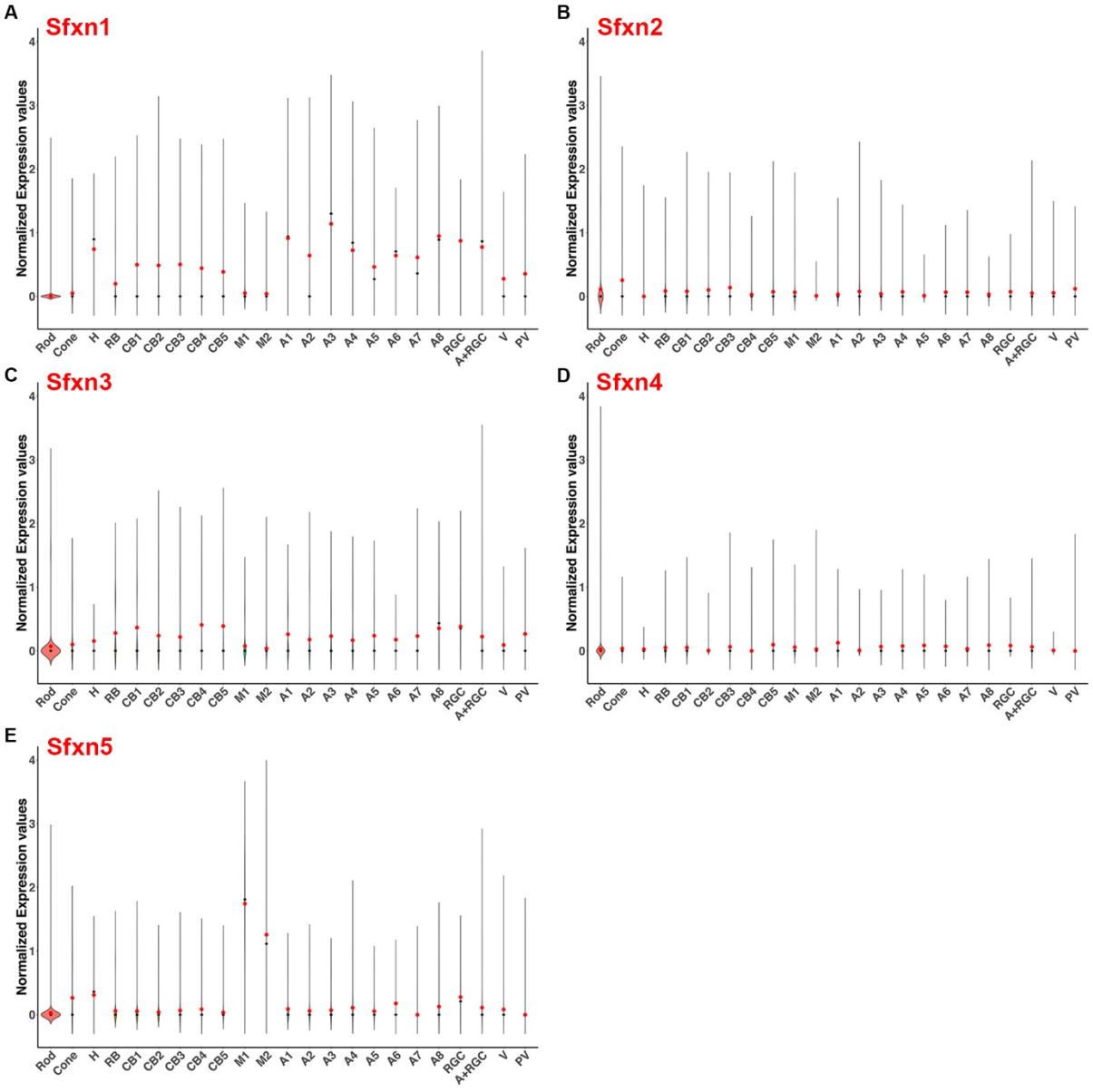

Fig. S8. Analysis of the expression of the different Sfxn homologs in different retinal cell types using single cell RNA sequencing. Violin plots showing normalized expression values for Sfxn1 (A), Sfxn2 (B), Sfxn3 (C), Sfxn4 (D) and Sfxn5 (E) in different cell types. Abbreviations: H - horizontal cells, RB – rod bipolar cells, CB – cone bipolar cells, A – amacrine cells, RGC – retinal ganglion cells, V – vascular cells, PV – perivascular cells.

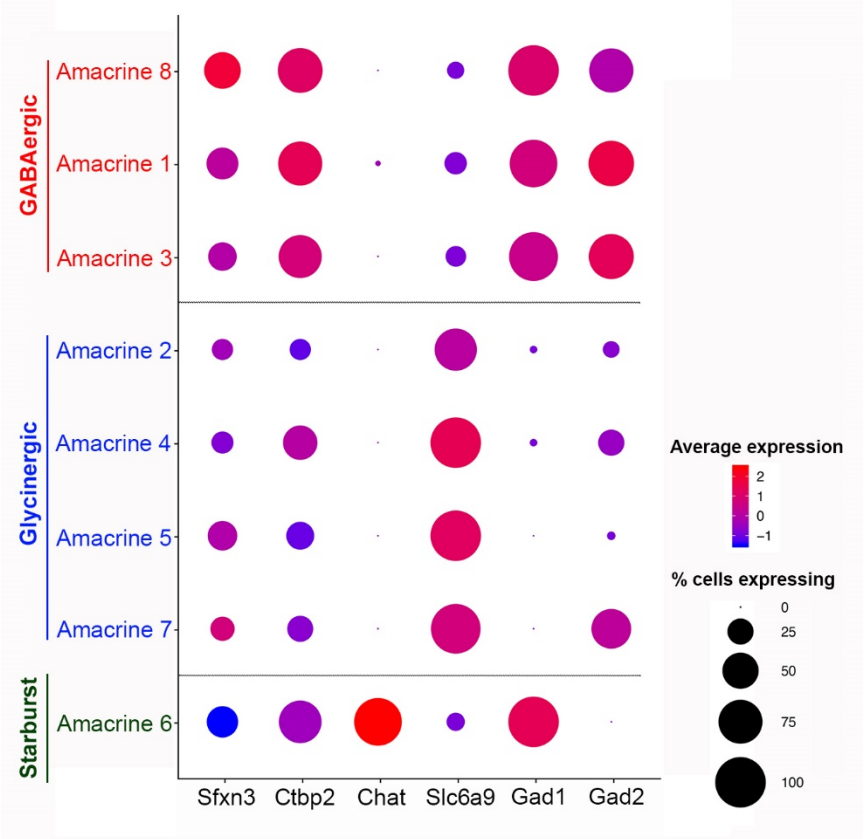

Fig. S9. Bubble plot of gene expression in amacrine clusters. Clusters 8, 1 and 3 show strong expression of the GABAergic markers Gad1 and Gad2. Meanwhile, clusters 2, 4, 5 and 7 show strong expression of the Glycinergic marker Slc6a9. Finally, cluster 6 shows an expression pattern classic for Starburst amacrine cells, with high Chat and Gad1 expression. Of interest, although several amacrine clusters had some expression of the ribbon synapse marker Ctbp2, it seemed to be highest in GABAergic amacrine clusters. Similarly, while multiple clusters had some expression of Sfxn3, expression seemed hightest in the GABAergic Amacrine 8 cluster.

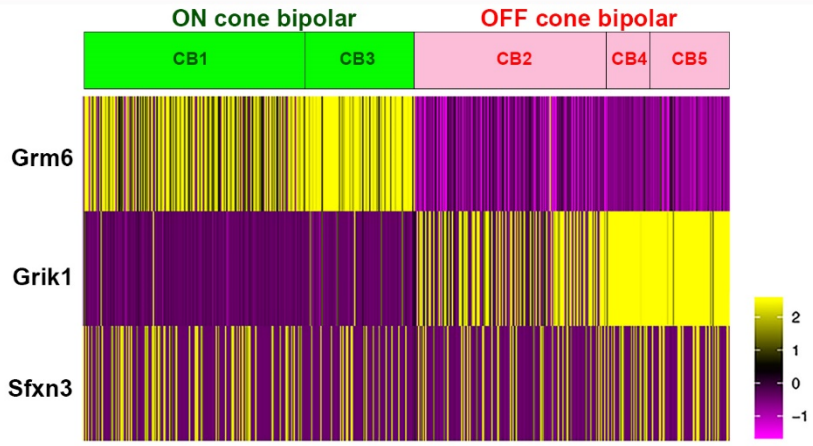

Fig. S10: Sfxn3 expression in cone bipolar (CB) cell clusters from Sfxn3+/+ mice. Clusters 1 and 3 show a strong expression of the ON-bipolar marker Grm6. On the other hand, clusters 2, 4 and 5 have a strong expression of the OFF-bipolar marker Grik1. Yet, Sfxn3 expression seems to be evenly distributed among ON and OFF clusters.

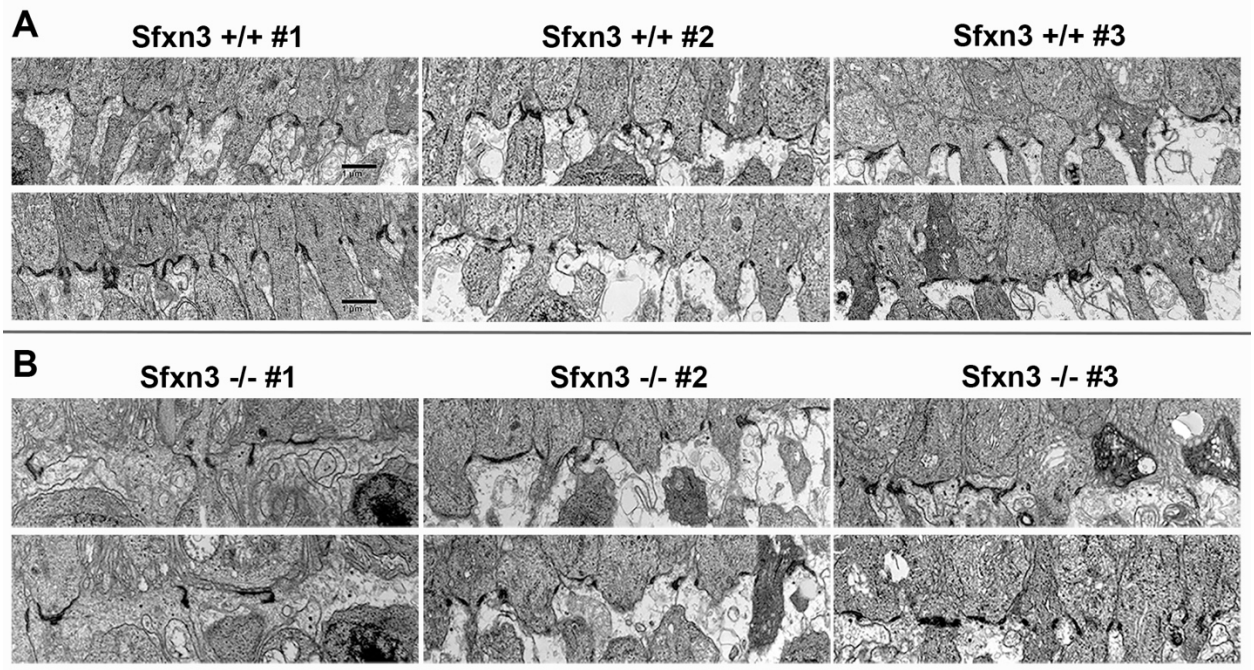

Fig. S11. Disruption of external limiting membrane (ELM) in Sfxn3 -/- mice. Electron microscopy images showing the electron dense ELM in three Sfxn3 +/+ controls eyes (A) and three Sfxn3 -/- eyes (B). Two EM fields (one on top of the other) are shown for each eye. Clear disruption of the Sfxn3 -/- ELM can be seen as disorganization and missing areas of electron dense adherens junctions.

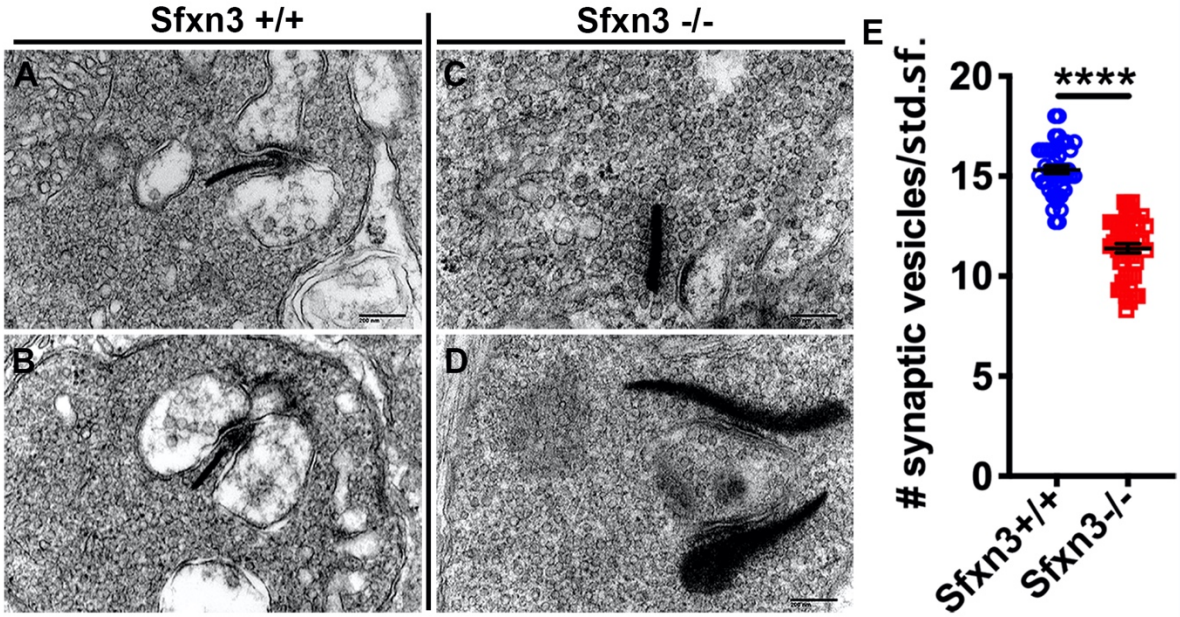

Fig. S12. Electron microscopy demonstrates a decrease in the number of vesicles in the outer plexiform layer synaptic terminals of Sfxn3 -/- (C,D) retinas compared to controls (A,B). This difference is statistically significant (E). Abnormal synaptic ribbons are also seen in the Sfxn3 -/- eyes. Vesicles were counted in standard subfields (std. sf.) measuring 200 nm x 200 nm in size.

Table S1. Identified gene-phenotype associations with literature support

#	Gene	Parameter	% change	log_{10}(p value)	Homozygous Affected	Mutation Type	Reference
1	Slc6a6	**2**	-62	-18	2/2	MS- PrD	S1-3
2	Vldlr	1,**3**	-48	-12	4/4	MS- PrD	S4-6
3	Tmem135	1,2,**3**	-53	-11	3/3	NS- PN	S7
4	Impdh1	**1**,2,3	-23	-9	3/3	NS- PN	S8,9
5	Epb41l2	2,**3**	-36	-9	2/2	CSAS-PN	S10,11
6	Arntl	1,2,**3**	-11	-7	3/3	MS- PrD	S12,13
7	Plxnb1	**1**	-12	-6	2/2	MS- PD	S14
8	Crx	**1**,2,**3**	-100	-5	9/9	NS- PN	S15-17
9	Cacna2d4	2,**3**	-23	-5	3/3	CSDS-PN	S18-20
10	Llgl1	1,2,**3**	-59	-11	1/1	MS-PB	S21
11	Cngb1	**3**	-53	-10	1/1	MS- PrD	S22,23

Our protocol identified 11 genes that have been reported to be associated to retinal development or function. The bottom two are genes that were found based on a single homozygous mouse. The parameters examined were: 1 = BM to ELM thickness on OCT, 2 = BM to ILM thickness on OCT, 3 = ONL thickness on OCT. We selected the parameter (shown in bold) with the largest "% change" (% difference in thickness in homozygous mutant mice compared to the aggregate of wild type (WT) and reference mice). The "% change" for that parameter is shown. Abbreviations: MS - missense, NS - nonsense, CSDS – critical splice donor site, PB – probably benign, PN – probably null, PD – possibly damaging, PrD – probably damaging.

	Sfxn1				Sfxn3				Sfxn5				Sfxn2				Sfxn4			
Cell	%e	Mean	SD	SEM	%e	Mean	SD	SEM	%e	Mean	SD	SEM	%e	Mean	SD	SEM	%e	Mean	SD	SEM
Rod	0.2	0.00	0.09	0.00	4	0.07	0.36	0.01	2	0.03	0.23	0.01	7	0.11	0.43	0.01	1	0.03	0.22	0.01
cone	4	0.05	0.25	0.03	10	0.10	0.31	0.03	27	0.27	0.45	0.05	25	0.25	0.47	0.05	4	0.04	0.18	0.02
H	89	0.74	0.40	0.13	44	0.15	0.19	0.06	56	0.31	0.34	0.11	0	0.00	0.00	0.00	11	0.03	0.08	0.03
RB	21	0.20	0.41	0.03	30	0.28	0.45	0.03	7	0.06	0.22	0.01	9	0.08	0.28	0.02	6	0.05	0.21	0.01
CB1	43	0.50	0.60	0.04	34	0.36	0.52	0.04	5	0.05	0.25	0.02	7	0.08	0.29	0.02	5	0.05	0.22	0.02
CB2	39	0.49	0.66	0.05	23	0.24	0.46	0.04	4	0.04	0.20	0.02	9	0.10	0.33	0.03	1	0.01	0.07	0.01
CB3	42	0.25	0.52	0.05	18	0.22	0.41	0.04	7	0.18	0.55	0.06	13	0.09	0.36	0.04	5	0.04	0.22	0.02
CB4	41	0.44	0.57	0.09	41	0.41	0.51	0.08	8	0.09	0.29	0.05	3	0.03	0.17	0.03	0	0.00	0.00	0.00
CB5	34	0.39	0.55	0.07	32	0.39	0.58	0.07	3	0.03	0.19	0.02	6	0.07	0.31	0.04	9	0.10	0.32	0.04
M1	6	0.60	0.64	0.05	10	0.08	0.39	0.03	96	0.18	0.50	0.04	8	0.08	0.28	0.02	8	0.06	0.21	0.02
M2	5	0.04	0.19	0.02	3	0.04	0.24	0.03	56	1.26	1.22	0.16	2	0.01	0.06	0.01	2	0.03	0.21	0.03
A1	79	0.91	0.61	0.05	38	0.26	0.35	0.03	13	0.09	0.24	0.02	5	0.03	0.16	0.01	21	0.13	0.26	0.02
A2	44	0.64	0.76	0.06	15	0.18	0.42	0.04	6	0.06	0.25	0.02	5	0.08	0.35	0.03	1	0.01	0.07	0.01
A3	83	1.14	0.68	0.07	30	0.23	0.38	0.04	10	0.07	0.22	0.02	4	0.04	0.20	0.02	10	0.07	0.20	0.02
A4	62	0.72	0.66	0.08	17	0.17	0.38	0.05	10	0.11	0.35	0.04	7	0.07	0.26	0.03	8	0.08	0.25	0.03
A5	50	0.46	0.54	0.07	33	0.24	0.36	0.05	8	0.06	0.20	0.03	2	0.01	0.08	0.01	13	0.09	0.23	0.03
A6	85	0.64	0.35	0.07	37	0.18	0.24	0.05	33	0.18	0.27	0.05	11	0.07	0.20	0.04	15	0.07	0.17	0.03
A7	50	0.61	0.67	0.13	21	0.23	0.47	0.09	0	0.00	0.00	0.00	7	0.07	0.25	0.05	4	0.03	0.17	0.03
A8	90	0.95	0.52	0.08	51	0.35	0.40	0.06	20	0.13	0.30	0.05	7	0.03	0.12	0.02	15	0.09	0.24	0.04
RGC	95	0.87	0.33	0.05	69	0.38	0.38	0.06	56	0.28	0.32	0.05	21	0.07	0.17	0.03	26	0.08	0.18	0.03
A + RGC	53	0.77	0.81	0.10	18	0.22	0.53	0.06	10	0.11	0.39	0.05	4	0.05	0.26	0.03	7	0.06	0.24	0.03
V	40	0.28	0.39	0.07	13	0.09	0.26	0.05	10	0.08	0.33	0.06	7	0.05	0.23	0.04	3	0.01	0.04	0.01
PV	29	0.35	0.66	0.25	29	0.27	0.46	0.17	0	0.00	0.00	0.00	14	0.12	0.32	0.12	0	0.00	0.00	0.00

Supplemental Table S2. Expression of Sfxn homologs in different cell subtypes. Expression was mostly seen for Sfxn1, 3 and 5 (thick black borders). Cell subtypes with %e (% of cells expressing the given Sfxn homologs) >50% are highlighted in yellow, while those with >30% are highlighted in green. The red boxes show cell subtypes that meet statistical significance for higher Sfxn3 expression compared to the average cell expression.